Hydrol. Earth Syst. Sci. Discuss., 8, 10095–10123, 2011
www.hydrol-earth-syst-sci-discuss.net/8/10095/2011/
doi:10.5194/hessd-8-10095-2011

Hydrology and Earth System Sciences Discussions

Multi-offset ground-penetrating radar imaging of a lab-scale infiltration test

A. R. Mangel[1], **S. M. J. Moysey**[1], **J. C. Ryan**[1], **and J. A. Tarbutton**[2]

[1]Environmental Engineering and Earth Sciences, Clemson University, 340 Brackett Hall, Clemson, SC 29634, USA
[2]Mechanical Engineering, Clemson University, 102 Fluor Daniel Building, Clemson, SC 29634, USA

Received: 31 October 2011 – Accepted: 4 November 2011 – Published: 15 November 2011

Correspondence to: A. R. Mangel (amangel@clemson.edu)

Published by Copernicus Publications on behalf of the European Geosciences Union.

Abstract

A lab scale infiltration experiment was conducted to evaluate the use of transient multi-offset ground-penetrating radar (GPR) data for characterizing dynamic hydrologic events in the vadose zone. A unique GPR data acquisition setup allowed sets of 21 traces at different offsets to be recorded every 30 s during a 3 h infiltration experiment. The result is a rich GPR data cube that can be viewed as multi-offset gathers at discrete moments in time or as common offset images that track changes in the GPR arrivals over the course of the experiment. These data allows us to continuously resolve the depth to soil boundaries while simultaneously tracking changes in wave velocity, which are strongly associated with soil water content variations. During the experiment the average volumetric water content estimated in the tank ranged between 10–30 % with discrepancies between the GPR results, moisture probe data, and 1-D numerical modeling on the order of 3–5 % (vol vol^{-1}), though the patterns of the estimated water content over time were consistent for both wetting and drying cycles. Relative errors in the estimated depth to a soil boundary located 60 cm from the surface of the tank were typically on the order of 2 % over the course of the experiment. During the period when a wetting front migrated downward through the tank, however, errors in the estimated depth of this boundary were as high as 25 %, primarily as a result of wave interference between arrivals associated with the wetting front and soil boundary. Given that our analysis assumed one-dimensional, vertical infiltration, this high error could also suggest that more exhaustive GPR data and comprehensive analysis methods are needed to accurately image non-uniform flow produced during periods of intense infiltration. Regardless, we were able to track the movement of the wetting front through the tank and found a reasonably good correlation with in-situ water content measurements. We conclude that transient multi-offset GPR data are capable of quantitatively monitoring dynamic soil hydrologic processes.

HESSD

8, 10095–10123, 2011

1 Introduction

Ground penetrating radar (GPR) has been established as a valuable tool for evaluating soil water content (Huisman et al., 2003). Surface-based radar reflection surveys are particularly appealing for this purpose as they can map large-scale regions that are relevant to field applications ranging from precision agriculture (Freeland et al., 1998; Lunt et al., 2005) to contaminant transport (Brewster et al., 1995). Several authors, including Lunt et al. (2005) and Grote et al. (2005), have shown that GPR reflection surveys can provide water content estimates with an accuracy comparable to traditional invasive, spatially limited methods, e.g., time-domain reflectometry (TDR) or neutron probes. A significant advantage of these probes over radar, however, is that they can provide reliable water content estimates with high-temporal resolution, e.g., at time scales capturing the dynamics of individual infiltration events. In contrast, almost all studies using GPR to quantitatively estimate water content have been performed under nearly steady-state hydraulic conditions or where changes in water content have been observed over long periods of time, e.g., seasonally, due to the significant effort and time required for data collection.

Most common methods for estimating water content from GPR are based on deriving wave velocity from arrivals identified in radar images (Huisman et al., 2003). For example, Lunt et al. (2005) mapped seasonal changes in water content over an 80×180 m area of a vineyard by evaluating variations in wave velocity determined from the traveltime of reflections produced by a clay layer of known depth, where the depth of the clay layer was inferred from borehole data. Water contents were then estimated from the velocities using a site-specific petrophysical equation. Following a different approach, Huisman et al. (2001) used changes in the traveltime of the direct groundwave in a wide angle reflection-refraction (WARR) survey to calculate lateral variations in wave velocity, which were subsequently transformed to near surface water content. Whether accurate wave velocities can be estimated from the groundwave during infiltration events has been put into question, however, by van der Kruk (2006) who showed

HESSD
8, 10095–10123, 2011

shallow, low-velocity waveguides, such as the region behind a wetting front, cause significant dispersion. In contrast, van Overmeeren et al. (1997) analyzed reflected and refracted wave arrivals in multi-offset data obtained from central midpoint (CMP) surveys to successfully determine both lateral and vertical variations in water content.

Traditional multi-offset GPR survey techniques, i.e., CMP or WARR, are appealing strategies for monitoring water content changes associated with one-dimensional infiltration as they are well established in the literature (Berard and Maillol, 2007; Fisher et al., 1992; Greaves et al., 1996; Grote et al., 2005) and can be easily put into practice with widely available commercial GPR systems. Analysis of the data from these surveys typically relies on normal moveout (NMO) corrections (Fisher et al., 1992), however, which assumes idealized, locally continuous reflector geometries. To overcome these limitations, Bradford (2008) used reflection tomography to obtain improved velocity estimates and GPR reflection images in areas with significant lateral heterogeneity. The intensive surveying required to collect data for reflection tomography, however, makes the approach challenging to implement at the short time scales associated with the dynamics of individual soil hydrologic events, such as infiltration in response to rainfall. Given that natural infiltration in soils can often be conceptualized as a one-dimensional process at field scales, it is not yet clear whether meaningful dynamic water content estimates can be obtained from multi-offset GPR using a NMO approach or whether more data intensive reflection tomography methods will need to be adopted.

There are relatively few examples in the literature that directly illustrate the influence of soil hydrology on surface-based GPR surveys (Freeland et al., 2006; Grasmueck et al., 2010; Grote et al., 2005; Haarder et al., 2011; Lambot et al., 2008; Moysey, 2010; Saintenoy et al., 2008; Truss et al., 2007). Truss et al. (2007) performed 3-D time-lapse GPR imaging of infiltration in an oolitic limestone that revealed macroscopic funnel flow effects. These authors also observed overall shifts in reflector traveltimes that were suggested to be caused by changes in soil moisture, but they did not provide direct estimates of water content. Haarder et al. (2011) used constant-offset GPR

HESSD
8, 10095–10123, 2011

surveys to monitor an infiltration experiment where dye was applied to mark preferential flow paths that were later identified when the site was excavated following the test. These authors concluded that wetting front non-uniformity and fingering complicated the GPR images noting impacts on both radar velocity and amplitudes, but preferential flow features themselves were not resolved. Grote et al. (2005) used constant-offset and CMP surveys to monitor changes in water content beneath a synthetic road bed during infiltration tests conducted over a period of approximately 35 weeks and found close agreement with gravimetric water content estimates. Moysey (2010) used a set of fixed antennas placed on the surface of a sand tank to show that changes in water content during wetting and drying events produce distinct arrival trajectories in transient constant offset GPR data. These data were then used to calibrate the parameters of a soil infiltration model. Because the antennas were maintained at a constant offset from each other in that work, however, it was not possible to directly determine subsurface velocity or estimate reflector depths using the GPR data alone. Despite the various hydrologic and geophysical insights provided by these studies, none has directly evaluated whether multi-offset imaging can be used to quantify water content changes in a dynamically changing soil environment at timescales typical of rainfall and irrigation events.

In this study we investigate whether NMO analysis of WARR surveys can be used to continuously monitor water content, track infiltration fronts, and image soil structure over the course of a short-term infiltration experiment. The experiment is conducted in a sand tank where water is applied uniformly to the surface while an automated positioning system moves a receiver antenna to 21 different positions above the tank. This unique approach to antenna positioning allows us to collect multi-offset images as approximate "snapshots" of the tank over time. Conceptualizing the data as a 3-D volume, i.e., with dimensions of GPR traveltime, antenna offset, and elapsed time since the start of the experiment, provides a rich space for enhanced analysis of transient processes that we expect will allow us to achieve reliable, high resolution monitoring of hydrologic events in soils.

HESSD
8, 10095–10123, 2011

2 Methods

2.1 Experimental procedures

The infiltration experiment was conducted in a 150 × 150 × 80 cm (L × W × H) wooden tank illustrated in Fig. 1. The tank was packed with a 60 cm layer of homogeneous, medium grained (0.25–0.5 mm) sand, below which was placed a 20 cm layer of gravel to allow for drainage. While packing the sand, fifteen Decagon EC-5 soil moisture probes were installed in the tank. The probes were placed in a central array at depths of 5, 10, 15, 25, 35, 45 and 55 cm and four lateral arrays, each with probes at depths of 15 and 45 cm. The probes recorded water content at 10 s intervals throughout the experiment. The depth distribution of initial water content prior to the experiment was evaluated using the probes and found to be at equilibrium assuming no vertical flow, though it was non-uniform due to redistribution of water during previous infiltration tests conducted in the tank (see Fig. 2).

The infiltration event was initiated by applying water to the sand surface using an irrigation grid consisting of a network of parallel (0.64 cm O.D. × 0.43 cm I.D.) polyethylene tubes. The tubes were spaced at 1 cm intervals and punctured every 1 cm to give a 1 × 1 cm grid of irrigation points over an area of 6750 cm^2. A peristaltic pump monitored by a flow meter provided control over the flux of water applied to the tank. The tubing was initially purged of air using a set of valves so that water could be applied uniformly to the surface of the tank as soon as the pump was turned on.

An automated radar imaging system was developed using LabVIEW (National Instruments, Austin, Texas) to achieve fast and accurate multi-offset antenna positioning for the WARR surveys performed during the experiment. A stationary transmitter antenna was placed on the irrigation grid 7 cm from one end of the tank while the receiver antenna was mounted 4 cm above the sand surface on a carriage that could move the length of the tank on an elevated track. The receiver antenna was moved using a belt drive (Pittman Express DC servo motor, Model GM9236S021-R1 and Pololu motor drive chip, Model MD01B), which had a 500 pulse per revolution encoder on the motor

HESSD
8, 10095–10123, 2011

to provide lateral positioning precision on the order of tenths of a millimeter. LabVIEW was interfaced with the GPR trigger to fire the transmitter whenever the receiver antenna was stopped at a desired survey position, though the radar's standard control software was run from a separate computer to collect the data.

The radar system used in the experiment was a PulseEKKO 1000 with 900 MHz antennas (Sensors and Software, Mississauga, Ontario, Canada). The transmitter antenna was fired at 21 different positions as the receiver was scanned across the tank with antenna offsets ranging from 0.44–0.9 m. Each round trip of the receiver antenna across the tank was completed in approximately 60 s, but data were collected in both directions so a complete 21 trace WARR survey was collected every 30 s during the experiment.

No water was applied to the tank for the first 8 min of the experiment to ensure that consistent GPR data could be obtained and to assess background conditions in the sand. Water was then applied at the surface of the tank by the irrigation grid for 65 min at a rate of 0.44 cm min^{-1}. After this time, the pump was turned off and an additional 107 min of recovery data were collected as water redistributed in the tank. A total of 6300 GPR traces were collected as 300 multi-offset WARR surveys during the experiment.

2.2 Normal moveout analysis of WARR surveys

Multi-offset GPR data are typically analyzed by applying normal moveout (NMO) corrections to determine the one dimensional velocity structure of the subsurface, e.g., see Yilmaz (1987) for details on NMO analysis and Fisher et al. (1992) for application of NMO to GPR. Using the NMO approach, the apparent (root mean square) velocity (V_{RMS}) of a wave traveling through the subsurface can be determined by assuming that the traveltime of a wave reflected from a subsurface interface increases in a well-defined way as the offset between transmitter and receiver antennas is increased. For a horizontal interface, the relationship between the two-way traveltime (t) to a reflector located at depth (z) and antenna offset (x) is linear when plotted as x^2 vs. t^2:

HESSD
8, 10095–10123, 2011

$$t^2 = \frac{x^2}{V_{RMS}^2} + \frac{4z^2}{V_{RMS}^2} \quad (1)$$

The first step in NMO analysis of WARR data is therefore to identify a coherent set of arrivals in a multi-offset image that represent the reflection response from a subsurface interface. The traveltimes of the reflected wave estimated at each different offset between the transmitter and receiver antennas can then be fit by Eq. (1), with the resulting slope and intercept of the best fit line yielding V_{RMS} and the depth of the reflector. Due to the mode of data collection used in this study, identification of coherent reflections can also be aided by reflection patterns that are apparent when the data are plotted as constant-offset gathers as illustrated by Moysey (2010). We emphasize, however, that the ability to constrain both subsurface velocity and reflector depth over time is a key advantage of multi-offset versus constant-offset GPR data.

The effective dielectric constant (κ) of the subsurface can be determined from velocity given Eq. (2), where c is the speed of light in a vacuum. The dielectric constant can then be used to determine the average water content (θ) of the subsurface using a petrophysical equation such as the Topp equation (Topp et al., 1980), which is given in Eq. (3). For an in depth review and description of current GPR theory and applications refer to Jol (2009).

$$\kappa = \left(\frac{c}{V_{RMS}}\right)^2 \quad (2)$$

$$\theta = -0.053 + 0.029\kappa - 5.5\times10^{-4}\kappa^2 + 4.3\times10^{-6}\kappa^3 \quad (3)$$

2.3 Numerical modeling

Numerical modeling of the infiltration experiment and GPR data was performed to improve the interpretation of the experimental results. Wetting and drying of the

HESSD
8, 10095–10123, 2011

sand associated with the infiltration experiment were simulated using HYDRUS-1D (Simunek et al., 2005), which is a one dimensional finite difference model that solves Richards's equation for unsaturated flow. The 0.60 m profile of sand was discretized into 1001 cells. Non-uniform initial soil moisture conditions were specified in the model based on the in-situ moisture probe readings observed at the beginning of the tank experiment (Fig. 2). The same flux schedule used in the experiment was specified as the upper boundary condition in the model and the bottom boundary was specified as a seepage face to capture the capillary barrier effect that occurs at the sand-gravel interface in the tank. The hydraulic properties used to represent the sand in the simulations are given in Table 1. The model was used to simulate the 180 min duration of the experiment. Observation points were specified to represent probe locations in the tank, whereas the full simulated depth profiles were used to drive the model of the GPR response over the course of the experiment.

The GPR simulations were performed using the finite difference time domain code implemented by Irving and Knight (2006) in MATLAB to solve Maxwell's equations in two dimensions. A cross-section of the true tank geometry parallel to the axis of the WARR surveys was used in the simulations. In addition to the sand, a layer of air outside the tank was also included in the model to allow for reflected and refracted waves at these boundaries to be captured within the simulations. Perfectly matched layer (PML) absorbing boundaries were specified around the model domain to eliminate additional spurious reflections. The vertical profile of dielectric permittivity for the sand within the tank was obtained by using the Topp equation, Eq. (3), to transform the water content profiles output from HYDRUS-1D. The electrical conductivity was set to constant values of 1×10^{-3} μSm^{-1} and 0 μSm^{-1} for the sand and air, respectively. The conductivity of the sand was chosen to be constant since we are focused here on the kinematics of wave migration, but we acknowledge that changes in saturation would also affect the amplitude of the waves. The magnetic permeability was set to a constant value of 1 Henry m^{-1} for the entire model domain. The source wavelet used in the simulations was the normalized first derivative of the Blackman-Harris window with

HESSD
8, 10095–10123, 2011

a dominant frequency of 900 MHz. See Irving and Knight (2006) for additional model details.

3 Results

3.1 Observations

Volumetric water content changes measured by the central array of embedded moisture probes over the course of the experiment are shown in Fig. 2. Though the probes were calibrated prior to the experiment, one obvious inconsistency in the data is that the probe located at 0.10 m depth is slightly drier than that at 0.05 m. The shallower probe still responds first once infiltration begins, however, and the downward migration of the wetting front is apparent from the sequential increase in water content at each of the deeper probes as the experiment progresses; the arrival of the wetting front at each probe is indicated by an × in Fig. 2. The increase in initial water content with depth is responsible for the increasing velocity of the wetting front toward the bottom of the tank apparent in Fig. 3. On average, however, the wetting front moves with an approximately constant velocity of 3.3 cm min^{-1} in the upper 35 cm of the tank. This velocity is generally consistent with the applied flux of 0.44 cm min^{-1}, when the fact that the unsaturated fraction of the sand controlling the wetting front velocity ranges between about 10–20 %. Data from the lateral arrays of probes installed at depths of 15 and 45 cm (not shown) indicate that the migration of the wetting front was not completely uniform across the tank; at both depths the standard deviation of the front arrival time for the five probes in each array was 2.6 min. All probes reached constant water contents near 30 % about 30 min into the experiment, indicating that steady state flow has been achieved. Subsequent drainage of the tank from top to bottom is also apparent in the probe data after irrigation was ceased 73 min into the experiment.

Changes in the GPR arrivals during the experiment are shown for three representative times in the multi-offset images in Fig. 4 and four representative antenna offsets in

HESSD
8, 10095–10123, 2011

the constant offset images in Fig. 5. Note that no processing other than dewow filtering and time zero correction has been performed on these data. Major arrivals that can be identified in the figures include the direct groundwave (A), a reflection from the bottom of the sand (B), and a reflection from the wetting front (C).

Although not used for the analysis in this study, we point out that the groundwave arrival (A) is difficult to identify at early experiment times due to interference from other arrivals, e.g. wetting front arrival. At later time, however, the groundwave is readily observed. There is also a loss of amplitude for the groundwave at large offsets and at all offsets the amplitude decreases during the period of irrigation, but rebounds slightly when the irrigation is terminated. While we have not evaluated the cause of these amplitude variations, they are consistent with changes in electrical conductivity associated with the varying water contents and interference between arrivals.

The reflection produced by the bottom of the sand layer (B) can be clearly identified during the majority of the experiment, but it is obscured during the infiltration period as the wetting front migrates downward (Figs. 4 and 5). A hyperbolic moveout of wave traveltime with antenna offset consistent with Eq. (1) can be seen in the multi-offset data, though interference is clearly apparent in Fig. 4b. For the constant offset images in Fig. 5, the reflection pattern observed through time is similar to that observed for the moisture probe data, though it is inverted due to the inverse relationship between water content and wave velocity. Given that this reflection represents a fixed boundary in the tank, it is an important test target for evaluating whether soil heterogeneities can be used in the analysis of GPR monitoring data obtained during infiltration experiments.

Though it is more difficult to identify in the GPR data, arrival C indicates a reflection associated with the wetting front that marks the boundary between the water content perturbation caused by the infiltration event and the drier background conditions of the tank. The wetting front reflection is difficult to identify in the constant-offset data at early times (8–10 min) due to interference with the groundwave (Fig. 5). At later times in the experiment (15–20 min) the wetting front arrival is still difficult to identify, though the cause of interference is hard to determine directly from the data. Numerical

HESSD
8, 10095–10123, 2011

modeling results indicate that reflections from the walls of the tank (indicated as arrival D) contribute to the interference. A loss of reflection amplitude caused by decreasing contrasts in dielectric constant across the wetting front as the interface moves into the region of higher water content near the bottom of the tank is also a factor. Lateral variability in the depth of the wetting front could be a third reason for difficulty in identifying a coherent reflection response in the multi-offset data given that variations in the propagation of the wetting front were observed across the tank with the moisture probes. It is difficult to directly infer the degree of lateral variability that occurred from the GPR data alone, however, given the single transmitter position used for the WARR survey in the experiment. Finally, the dry soil conditions ahead of the front allow for faster wave velocities in this region, which would be expected to produce refracted waves, though such arrivals were not readily identified in the data.

3.2 NMO analysis of GPR arrivals

The arrival most readily analyzed by NMO analysis is the reflection produced at the interface between the sand and gravel near the bottom of the tank. The changes in traveltime for this arrival over the course of the experiment are associated with variations in velocity caused by increases and decreases in the net volume of water stored in the sand. The reflection traveltimes picked from the multi-offset images were used with Eq. (1) to estimate the average (RMS) wave velocity within the tank throughout the duration of the experiment. The dielectric constant was then determined with Eq. (2) and water content values shown in Fig. 6a were obtained from the Topp equation, Eq. (3).

Despite the vertical variability of water content in the tank, Fig. 6a shows that the trend in the depth-averaged water content estimated from the probes and that determined from velocity analysis of the reflection from the sand bottom are in reasonably good agreement. The GPR results generally underestimate the probe data by about 3 % (vol vol^{-1}), but not by a difference of more than 5 % (vol vol^{-1}). The numerical modeling results, also shown in Fig. 6a, similarly capture the overall patterns of depth-averaged water content in the tank derived from both the water contents simulated by

HESSD
8, 10095–10123, 2011

HYDRUS-1D and NMO analysis of the synthetic GPR data. In contrast to the empirical data, it is notable that for the simulations the water contents derived from the NMO analysis overestimate the average water content. Given that the numerical simulations capture the interaction between the propagating waves and water content variations within the tank, this discrepancy implies that the water content errors are not associated with a general phenomenon such as preferential sampling of fast versus slow zones in the tank. Rather, the observed water content errors are more likely associated with a bias in picking the reflection arrival times in this particular experiment.

NMO analysis can also provide estimates for the depth to the interface causing the bottom of tank reflections, i.e., the thickness of the sand layer in the tank, which are shown in Fig. 6b. The average depth to the bottom of the sand layer estimated over the course of the experiment is 58.7 cm, which is a 2 % error relative to the true sand thickness of 60.0 cm. During the infiltration period, however, a significant amount of variation was observed in the estimates of the depth to the interface. Errors ranged from an underestimate of the interface depth of 15 cm (25 % error) to an overestimate of 5 cm (8 % error). Although the errors are not as large for the analysis of the synthetic data, they are still most significant during the infiltration period implying that even under optimal conditions it can be challenging to obtain accurate depth estimates from GPR during highly dynamic subsurface events. While we emphasize that care should be taken in interpretation of such results and that further research could lead to reduced errors, we note that for many practical purposes a reasonable estimate of interface depth can be achieved.

Despite the challenges in identifying the wetting front reflection discussed earlier, it is possible to approximately track this arrival in the GPR data by simultaneously considering arrival trajectories at multiple offsets. NMO analysis can then be used to estimate both the depth to and water content above the wetting front in the tank. The estimated EM wave velocity behind the wetting front is relatively constant over time with a value of 0.08–0.1 m ns^{-1} in the wetted part of the tank. This range of velocity corresponds to water contents of 20–27 % (vol vol^{-1}), which is somewhat lower that the range of 26–34 %

HESSD
8, 10095–10123, 2011

observed with the moisture probes. The water content behind the wetting front estimated from the synthetic GPR data ranged between 18–21 % (vol vol^{-1}), which again underestimated the actual value of 22–28 % (vol vol^{-1}) obtained from HYDRUS-1D. In addition to these errors in water content, Fig. 3 shows that the NMO analysis consistently underestimated the depth of the wetting front for both the empirical and modeled data, especially in the deeper two-thirds of the tank. Regardless, the overall downward trend of the wetting front is similar to that observed for the water content probes. Based on the GPR data the wetting front appears to reach the bottom of the sand layer in the tank between 25–30 min into the experiment (Fig. 3), which is generally consistent with the time that water was observed to discharge from the tank drain 26 min into the experiment. The average downward wetting front velocity estimated from the arrival time of the front reflection at the bottom of the tank is roughly 2.0–2.4 cm min^{-1}, which is somewhat lower than but comparable to the rate calculated from the moisture probes (3.3 cm min^{-1}). Overall, the analyses of the empirical and simulated data suggest that NMO analysis provides some insight about wetting front migration during an infiltration event, but falls short of providing accurate estimates of water content, front position, and velocity in this experiment.

4 Discussion

One of the key challenges identified in the NMO analysis was that wave interference between different GPR arrivals complicated estimation of reflection traveltimes from the data. In this experiment there are a number of arrivals other than the primary reflection from the wetting front and bottom of the sand layer that could have contributed to complexity in the observed data, including: (1) waves reflected from the wetting front or bottom of the tank that are subsequently refracted in the air at the surface of the tank, (2) reflection multiples within the wetting front, (3) refracted arrivals associated with high velocity zones ahead of the wetting front, (4) reflections from the side boundaries of the tank, and (5) reflections from the embedded moisture probes. We used the

HESSD
8, 10095–10123, 2011

numerical simulations to aid in evaluating how arrivals 1–4 might have affected our interpretations of the hydrologic responses. Figure 7 illustrates the propagation of the radar waves as they interact with the tank for different hydrologic conditions before and during, the infiltration event; simulations during the recovery period are similar to those observed prior to infiltration.

As the reflection from the bottom of the tank returns to the tank surface an air refracted wave is generated. At large offsets this wave arrives slightly before the bottom of tank reflection causing a shorter apparent travel time giving higher apparent velocity in the tank, which translates into an underestimate for water content (Fig. 6a). While this is consistent with the GPR data, this source of error remains inconclusive since the GPR model over estimates water content.

The modeled wavefield is very complicated while the wetting front is propagating downward through the tank (Fig. 7b). Evidence of multiple reflections from the wetting front can be seen in the simulations. These multiples do not appear to create the shingled appearance in the data suggested by van der Kruk et al. (2009) as an indicator for dispersive waves caused by the presence of a low velocity wave guide. The difference could be related to a number of factors, such as gradients in moisture content in the tank rather than a sharp lithologic boundary, changes in the wetting front depth over time, or interference from other arrivals. The shape of the groundwave is clearly affected at larger offsets, however, suggesting that dispersion is a factor in the data. This is one reason that we have chosen not to analyze the groundwave in this work.

It is also apparent from the simulation results in Fig. 7b that the wave transmitted across the wetting front is refracted and begins to propagate ahead of the reflected waves, ultimately creating a head wave that interferes with the wetting front reflection. The impact of this interference is dependent on the depth of the wetting front. At early times in the experiment, when the thickness of the wetted layer is small, there could be sufficient separation between the arrivals to identify the refraction at large receiver offsets. At later times in the experiment, when the wetting front is deeper in the tank, the arrivals would interfere with each other. Some of these effects may be present in

HESSD
8, 10095–10123, 2011

our data, though from the constant-offset images in Fig. 5 it appears that that a larger effect is the overall loss of reflection amplitude as the wetting front moves into wetter regions near the bottom of the tank due to lower dielectric contrasts. Overall, it is clear that complexities associated with dispersion and refraction associated with the wetting front make the analysis of the reflection from this interface complicated. We would have had extreme difficulty in identifying the wetting front reflection at all if not for the fact that we could use the 3-D radar cube to simultaneously interpret transient responses from multiple offsets as the front propagated downward.

Reflections from the walls of the tank also complicate the data. For example, in Fig. 7, a secondary wave created by a reflection from the left wall of the tank follows the primary direct wave emitted by the transmitter. This scattered energy along with arrivals associated with the wetting front are likely reasons why we had difficulty in accurately estimating the depth of the tank during the period when infiltration was occurring (Fig. 4). When simulations were performed where the tank boundaries were removed (results not shown), the wavefield becomes more coherent and easier to interpret. Also clearly observed in the tank data is a reflection arising from one of the embedded soil moisture probes, which further adds to the noise in the images (Fig. 4). In general, however, the impact of these types of scattering could be reduced by migrating the GPR data.

Despite the fact that the NMO analysis used in this work was relatively simple, that our modeling assumption of a laterally-uniform wetting front is likely inaccurate based on the moisture probe data, and that there was substantial noise in the GPR data generated by scattering and refractions, we still obtained a good deal of quantitative insight into the macroscopic flow processes occurring in the tank using transient WARR surveys. It is possible that full 3-D GPR imaging, where both the transmitter and receiver antennas are moved, could capture more details related to local variations in flow, i.e., non-uniformity of the wetting front or other preferential flow processes. For example, Truss et al. (2007) were able to capture the interaction between the wetting front and a meter-scale structural feature (sand-filled hole) that channeled flow during

HESSD
8, 10095–10123, 2011

an experiment in the Miami Oolite. Both the 3-D GPR monitoring studies by Truss et al. (2007) and Haarder et al. (2011) suggest, however, that directly capturing small-scale preferential flow features can be challenging. Haarder et al. (2011) were able to observe changes in reflection amplitudes that they interpreted to be caused by ponding associated with funnel flow, but they were not able to interpret individual small-scale preferential flow features directly from the GPR data. These authors concluded that GPR was useful for identifying patterns associated with large-scale flow processes, which have been observed by both Haarder et al. (2011) and Truss et al. (2007) to cause macroscopic changes in water content that produced shifts in the traveltime of reflections associated with soil heterogeneities. This is consistent with our results, where we have found that a reflection from a subsurface interface, i.e., the sand-gravel boundary at the bottom of the tank, could provide reliable estimates of average water content over time. The complexity of the GPR response associated with the wetting front, the potential for preferential flow at scales below the resolution of GPR, and the quantitative consistency of water content estimates observed over both wetting and drying events in this study suggests that soil reflectors, i.e., physical contrasts in subsurface materials, are a critically important tool for quantitatively monitoring infiltration events.

Given that our experiment was intentionally designed to represent a simple soil environment with a single interface, it remains an open question whether our success in monitoring infiltration using the NMO approach could be achieved in more complicated environments. We acknowledge that acquiring more data, e.g., full-resolution 3-D GPR surveys with multiple antenna offsets, will always hold more potential for resolving the details of infiltration in the subsurface. The time required to perform these surveys, however, is still a limiting factor; e.g., Truss et al. (2007) report that in their study it required 50 min to perform each constant offset survey over a 10×10 m area using a custom single channel GPR that was integrated with an advanced positioning system specifically for 3-D surveying. In contrast, multi-channel GPR systems amenable to fast WARR surveying over large areas are commercially available "off-the-shelf" at

HESSD
8, 10095–10123, 2011

a reasonable cost. If NMO analysis of transient WARR data could be shown to provide reliable average water content estimates in heterogeneous soils, it would open a new opportunity to provide critically important data to hydrologists and soil scientists working at catchment scales.

5 Conclusions

A lab-scale infiltration and redistribution experiment was performed to constrain subsurface structures and water content variability with time. The unique form of automated transient multi-offset surveying used in this study allowed us to collect a 3-D GPR data cube that can be viewed as either multi-offset or constant offset gathers. Normal move-out (NMO) analysis of reflections related to the bottom of a sand layer were used to independently estimate the mean radar velocity and average soil water content of the tank over the course of the experiment and provided agreement with averaged moisture probe measurements and numerical modeling results on the order of 3–5 % (vol vol^{-1}). It was also possible to independently determine the depth to the bottom of the sand layer with an average error of about 3 % and maximum error on the order of 25 %, which occurred as the infiltrating wetting front approached this interface.

The movement of the wetting front reflection was also visible in the GPR data. Analysis of this arrival allowed us to track the depth to the wetting front in the tank over the course of the experiment, which showed reasonably good agreement with moisture probe observations and modeling results obtained from the model HYDRUS-1D. The challenges in identifying this arrival are numerous, however, which illustrated the benefit of simultaneously using the multi-offset and constant offset gathers to interpret the wetting front response as a reflection surface within the 3-D GPR data cube. Despite the fact that the moisture probe data indicated that the wetting front was non-uniform, we had a reasonable degree of success in capturing its behavior by assuming that it was laterally homogeneous. Further investigation is needed to more fully assess the

HESSD
8, 10095–10123, 2011

errors of this one-dimensional conceptualization and determine the additional value of collecting 3-D GPR data to quantify non-uniform flow.

This study illustrates the potential of transient multi-offset reflection surveys for improving the characterization of vadose zone dynamics. The key advantage of the approach is that it is possible to estimate wave velocity and constrain the depth of subsurface structures directly from the GPR data without the need for supporting data, such as boreholes to independently constrain the depth to reflectors. Changes in water content can then be obtained if a petrophysical relationship between dielectric constant and water content can be estimated for the soil. Given that multi-offset data can be collected quickly in the field using commercially available equipment, the results of this study suggest that there is significant opportunity for non-invasive monitoring of soil moisture dynamics over catchment scales at time scales relevant to individual hydrologic events, if strong radar reflectors exist within the soil profile. Improved characterization of the hydrologic state of the subsurface at catchment scales will ultimately lead to a better understanding of vadose zone processes and advances in soil infiltration models.

Acknowledgements. This material is based upon work supported by, or in part by, the U.S. Army Research Laboratory and the U.S. Army Research Office under grant number W911NF-08-1-0370.

References

Berard, B. A. and Maillol, J.-M.: Multi-offset ground penetrating radar data for improved imaging in areas of lateral complexity – application at a native American site, J. Appl. Geophys., 62, 167–177, 2007.

Bradford, J. H.: Measuring water content heterogeneity using multifold GPR with reflection tomography, Vadose Zone J., 7, 184–193, 2008.

Brewster, M. L., Annan, A. P., Greenhouse, J. P., Kueper, B. H., Olhoeft, G. R., Redman, J. D., and Sander, K. A.: Observed migration of a controlled DNAPL release by geophysical methods, Ground Water, 33, 977–987, 1995.

HESSD

8, 10095–10123, 2011

Fisher, E., McMechan, G. A., and Annan, P.: Acquisition and processing of wide-aperture ground-penetrating radar data, Geophysics, 57, 495–504, 1992.
Freeland, R. S., Yoder, R. E., and Ammons, J. T.: Mapping shallow underground features that influence site-specific agricultural production, J. Appl. Geophys., 40, 19–27, 1998.
Freeland, R. S., Odhiambo, L. O., Tyner, J. S., Ammons, J. T., and Wright, W. C.: Nonintrusive mapping of near-surface preferential flow, Appl. Eng. Agric., 22, 315–319, 2006.
Grasmueck, M., Marchesini, P., Eberli, G. P., Zeller, M., and VanDam, R. L.: 4D tracking of water infiltration in fractured high-porosity limestone, 2010 13th International Conference on Ground Penetrating Radar, Issue Date 21–25 June 2010, 1–6, 2010.
Greaves, R. J., Lesmes, D. P., Lee, J. M., and Toksoz, M. N.: Velocity variations and water content estimated from multi-offset ground-penetrating radar, Geophysics, 61, 683–695, 1996.
Grote, K., Hubbard, S., Harvey, J., and Rubin, Y.: Evaluation of infiltration in layered pavements using surface GPR reflection techniques, J. Appl. Geophys., 57, 129–153, 2005.
Haarder, E. B., Looms, M. C., Jensen, K. H., and Nielsen, L.: Visualizing unsaturated flow phenomena using high-resolution reflection ground penetrating radar, Vadose Zone J., 10, 84–97, 2011.
Huisman, J. A., Sperl, C., Bouten, W., and Verstraten, J. M.: Soil water content measurements at different scales: accuracy of time domain reflectometry and ground-penetrating radar, J. Hydrol., 245, 48–58, 2001.
Huisman, J. A., Hubbard, S. S., Redman, J. D., and Annan, A. P.: Measuring soil water content with ground penetrating radar, Vadose Zone J., 2, 476–491, 2003.
Irving, J. and Knight, R.: Numerical modeling of ground-penetrating radar in 2-D using MATLAB, Comput. Geosci., 32, 1274–1258, 2006.
Jol, H. M.: Ground Penetrating Radar: Theory and Applications, Elsevier, Slovenia, 2009.
Lambot, S., Binley, A., Slob, E., and Hubbard, S.: Ground-penetrating radar in Hydrogeophysics, Vadose Zone J., 7, 137–139, 2008.
Lunt, I. A., Hubbard, S. S., and Rubin, Y.: Soil moisture content estimation using ground-penetrating radar reflection data, J. Hydrol., 307, 254–269, 2005.
Moysey, S.: Hydrologic trajectories in transient ground-penetrating radar reflection data, Geophysics, 75, 211–219, 2010.
Saintenoy, A., Schneider, S., and Tucholka, P.: Evaluating ground-penetrating radar use for water infiltration monitoring, Vadose Zone J., 7, 208–214, 2008.

HESSD
8, 10095–10123, 2011

Simunek, J., van Genuchten, M. T., and Sejna, M.: HYDRUS 1D Code for simulating the one-dimensional movement of water, heat, and multiple solutes in variably saturated porous media, Department of Environmental Sciences and University of California Riverside, US Salinity Laboratory, USDA, ARS, Riverside, CA, 2005.

Topp, G. C., Davis, J. L., and Annan, A. P.: Electromagnetic determination of soil water content: measurements in coaxial transmission lines, Water Resour. Res., 16, 574–582, 1980.

Truss, S., Grasmueck, M., Vega, S., and Viggiano, D. A.: Imaging rainfall drainage within the Miami oolitic limestone using high-resolution time-lapse ground-penetrating radar, Water Resour. Res., 43, W03405, doi:10.1029/2005WR004395, 2007.

van der Kruk, J.: Properties of surface waveguides derived from inversion of fundamental and higher mode dispersive GPR data, IEEE T. Geosci. Remote, 44, 2908–2915, 2006.

van Overmeeren, R. A., Sariowan, S. V., and Gehrels, J. C.: Ground penetrating radar for determining volumetric soil water content; results of comparative measurements at two test sites, J. Hydrol., 197, 316–338, 1997.

Yilmaz, O.: Seismic data processing, SEG Investigations in Geophysics 2, Society of Exploration Geophysicists, Tulsa, OK, 1987.

HESSD

8, 10095–10123, 2011

Table 1. Sand hydraulic parameters used in HYDRUS-1D simulations.

Residual Water content Θ_r [vol. vol.$^{-1}$]	Saturated Water Content Θ_s [vol. vol.$^{-1}$]	Air-entry Parameter α [cm^{-1}]	Shape Parameter n [–]	Saturated Hydraulic Conductivity K_s [cm min^{-1}]
0.06	0.38	0.058	4.09	4.6

HESSD
8, 10095–10123, 2011

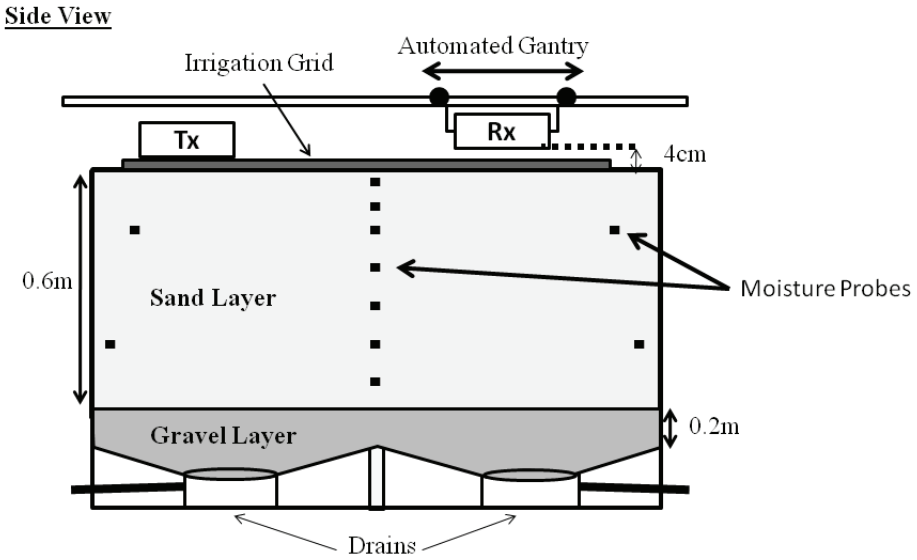

Fig. 1. Experiment setup for lab-scale infiltration experiments.

HESSD
8, 10095–10123, 2011

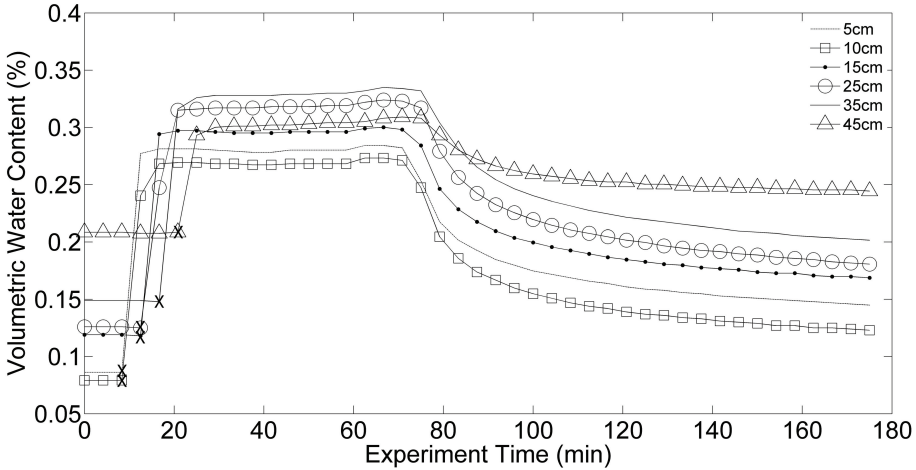

Fig. 2. Data from soil moisture probes located in the central array of the sand tank.

HESSD
8, 10095–10123, 2011

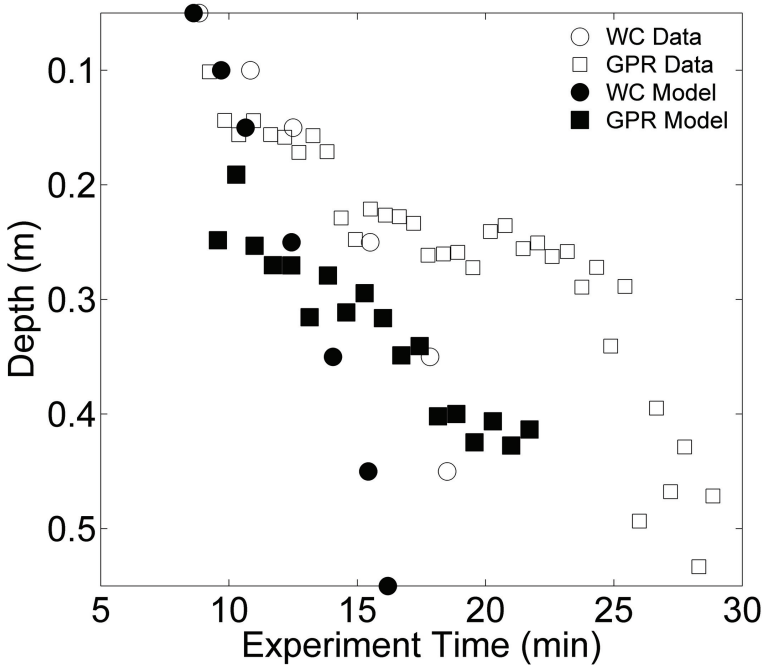

Fig. 3. Estimated depth to the wetting front based on data from water content probes, GPR, and simulation results.

HESSD
8, 10095–10123, 2011

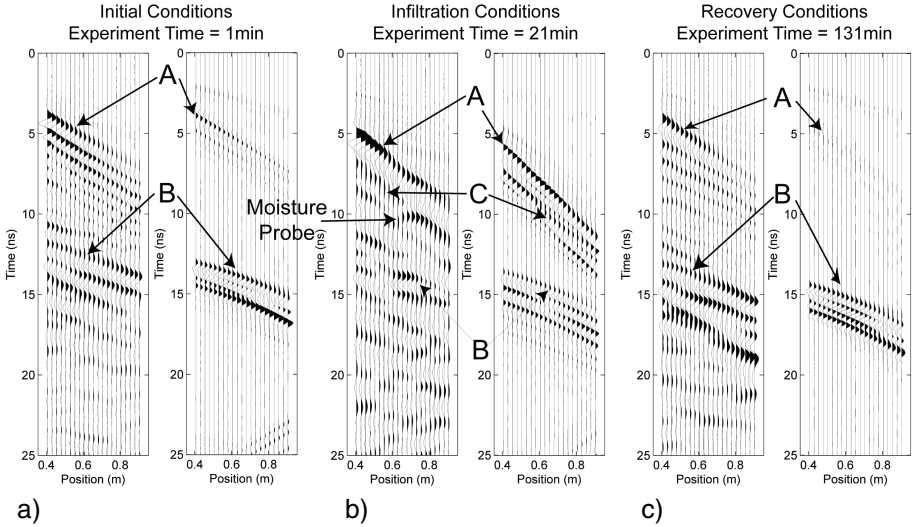

Fig. 4. Multi-offset sections for initial conditions **(a)**, infiltration time **(b)**, and recovery time **(c)** showing the groundwave (A), bottom of tank reflection (B), the wetting front reflection (C) and a diffraction arising from an in-situ moisture probe.

HESSD
8, 10095–10123, 2011

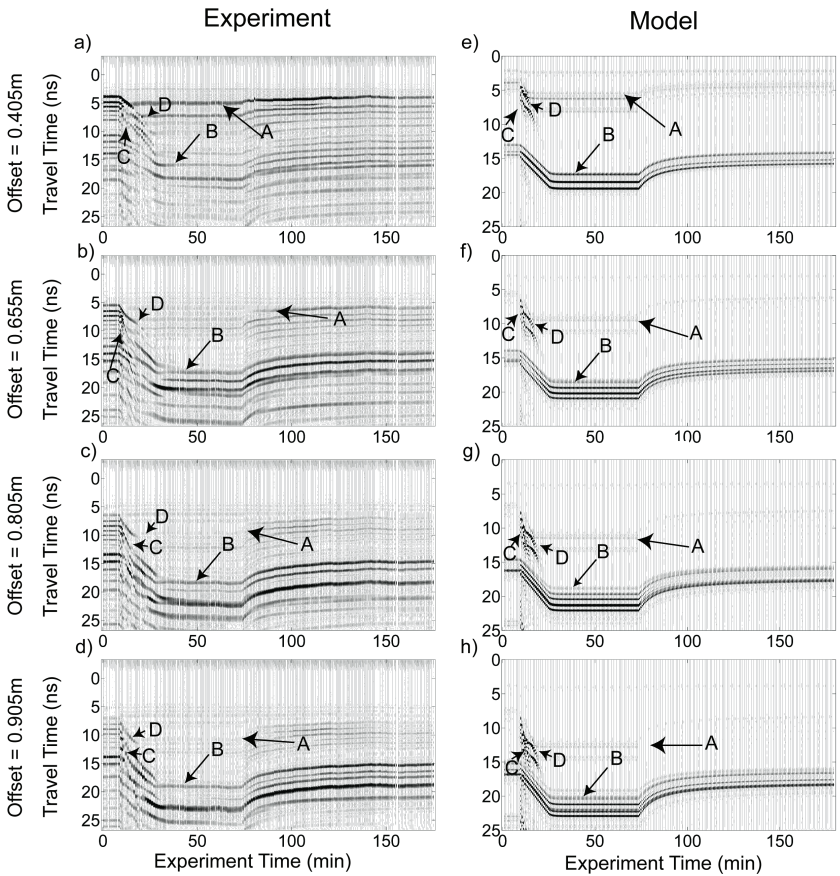

Fig. 5. Common offset projections for 4 of the 21 offsets of the experiment and model. Pointed out in the data are the groundwave (A), bottom of tank (sand-gravel interface) reflection (B), and wetting front reflection (C).

HESSD
8, 10095–10123, 2011

Multi-offset ground-penetrating radar imaging of a lab-scale infiltration test

A. R. Mangel et al.

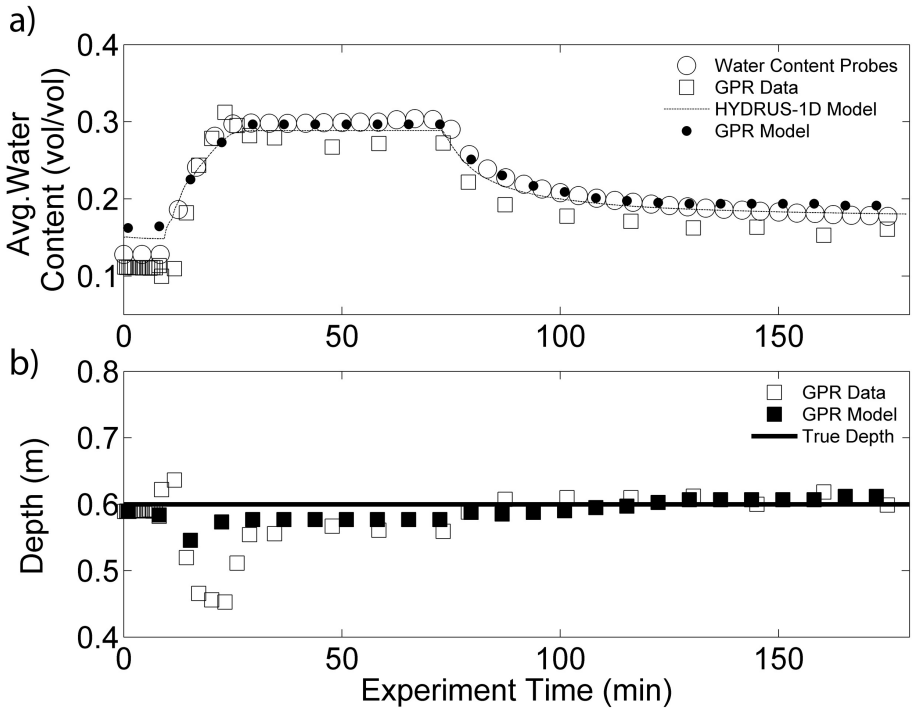

Fig. 6. **(a)** Average water content during the experiment estimated using the bottom of tank reflection in observed and simulated GPR data, moisture probes, and flow modeling with HYDRUS-1D. **(b)** Depth to reflector estimated from bottom of tank reflection for both GPR data and model.

HESSD
8, 10095–10123, 2011

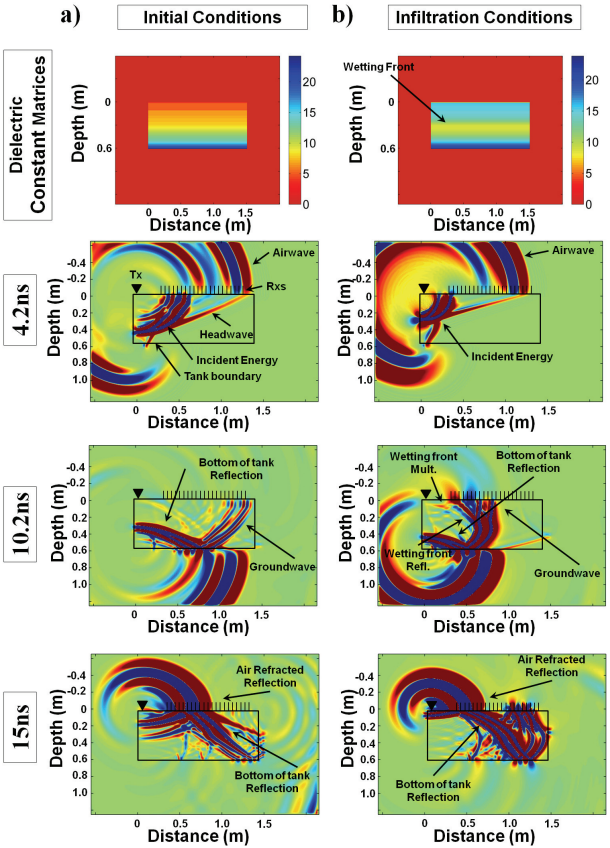

Fig. 7. Propagation of radar waves during iterations of the 2-D radar model showing evolution of radar wavefield through time for initial and infiltration conditions.

HESSD
8, 10095–10123, 2011

Multi-offset ground-penetrating radar imaging of a lab-scale infiltration test

A. R. Mangel et al.